Maximum entropy principle analysis in network systems with short-time recordings

Zhi-Qin John Xu,[1] Jennifer Crodelle,[2] Douglas Zhou,[3,*] and David Cai[1,2,3,4]

[1]*NYUAD Institute, New York University Abu Dhabi, Abu Dhabi, United Arab Emirates*
[2]*Courant Institute of Mathematical Sciences, New York University, New York, New York, USA*
[3]*School of Mathematical Sciences, MOE-LSC and Institute of Natural Sciences, Shanghai Jiao Tong University, Shanghai, P.R. China*
[4]*Center for Neural Science, New York University, New York, New York, USA*

In many realistic systems, maximum entropy principle (MEP) analysis provides an effective characterization of the probability distribution of network states. However, to implement the MEP analysis, a sufficiently long-time data recording in general is often required, e.g., hours of spiking recordings of neurons in neuronal networks. The issue of whether the MEP analysis can be successfully applied to network systems with data from short-time recordings has yet to be fully addressed. In this work, we investigate relationships underlying the probability distributions, moments, and effective interactions in the MEP analysis and then show that, with short-time recordings of network dynamics, the MEP analysis can be applied to reconstructing probability distributions of network states that is much more accurate than the one directly measured from the short-time recording. Using spike trains obtained from both Hodgkin-Huxley neuronal networks and electrophysiological experiments, we verify our results and demonstrate that MEP analysis provides a tool to investigate the neuronal population coding properties for short-time recordings.

I. INTRODUCTION

Binary-state models have been used to describe the activity of nodes in many network systems, such as neuronal networks in neuroscience [1–3]. Understanding the distribution of network binary-state dynamics is important in unveiling underlying network function, especially in neuroscience, where both theoretical and experimental results indicate that populations of neurons perform computations probabilistically through their firing patterns [4,5]. For instance, statistical distributions of neuronal network firing patterns have been shown to perform awake replays of remote experiences in rat hippocampus [5]. Therefore, studying the characteristics of neuronal firing pattern distributions will help to understand how neuronal networks encode information [6]. However, this is a difficult task, since the number of all possible network states grows exponentially as the network size increases, i.e., 2^n for a network of n binary-state nodes. This high dimensionality presents a challenge in directly measuring the distribution of network states in electrophysiological experiments, especially for the case of *in vivo* measurements on awake animals, thus, the difficulty in understanding coding schemes in neuronal networks.

The maximum entropy principle (MEP) analysis is a statistical method used to infer the least-biased probability distribution of network states by maximizing the Shannon entropy with given constraints, i.e., moments up to certain order [7]. The inferred probability distribution is called the MEP distribution. For example, under constraints of the first two-order moments, the second-order MEP distribution gives rise to an accurate estimate of the statistical distribution of network states in many scientific fields, e.g., neuroscience [1–3,8,9], biology [10–12], imaging science [13], economics [14,15], linguistics [16], anthropology [17], and atmosphere-ocean science [18]. However, the debate on the sufficiency of the second-order MEP (pairwise sufficiency) has been ongoing. For example, empirical studies found that the second-order MEP distribution is no longer sufficient for networks of large sizes (e.g., ∼100 neurons [19]), networks over fine scales (i.e., local clusters of neurons within $300\,\mu m$ [20]), and ongoing neuronal avalanches in the alert monkey and evoked visual responses in the anesthetized cat [21]. A series of studies investigated this pairwise sufficiency [22–26], such as how the pairwise sufficiency depends on the inputs [23,24]. Meanwhile, methods have also been developed to account for high-order effective interactions in the MEP analysis when the pairwise sufficiency fails [19,27–29]. For example, a method [29] was recently proposed to adaptively identify the specific pairwise and higher-order moments and it is able to capture cortical-like distributions of population spiking patterns.

However, a practical and important issue remains unclear: How well does the second-order MEP analysis perform based on a short-time recording? This is important because a very long recording is often required to carry out the MEP analysis, e.g., hours for a network of 10 neurons [1]. Specifically, to perform high-order MEP analysis, an extremely long recording is required, e.g., 24–30 h [19]. These long recordings are usually impractical to achieve due to cost or capability. For example, physiological constraints such as fatigue of neurons makes it very difficult to record the state of neuronal networks over a long time, especially *in vivo* recordings on awake animals. Meanwhile, data obtained by short-time recordings poorly captures many activity states, leading to incorrect descriptions

*zdz@sjtu.edu.cn

for the probability distribution of network states. The insufficient measurements due to short-time recordings could lead to a misunderstanding of information coding structure embedded in network activity states [20]. Therefore, it is important to estimate an accurate probability distribution of network states from short-time recordings where many network activities are under-represented.

In this work, we demonstrate that, compared with the probability distribution directly measured from a short-time recording, the second-order MEP analysis, performed based on data measured from a short-time recording, can give rise to a more accurate estimate of the probability distribution of network states. To achieve this, we first show that all moments and all effective interactions can equivalently represent a probability distribution of network states for a general network of any size. Next, we use the above equivalent representations to rationalize that low-order MEP analysis is capable of giving rise to an accurate estimate of the probability distribution of network states from a short-time recording.

Although the procedure described in this work can be applied to any network with binary dynamics, here we use spike trains obtained from both Hodgkin-Huxley (HH) neuronal network dynamics simulations and electrophysiological experiments to investigate whether the MEP analysis can accurately estimate the probability distribution of network states from short-time recordings. We also quantitatively study how the performance of MEP analysis with short-time recordings depends on the length of recording time and the number of neurons. Our results show that in both numerical simulation data and electrophysiological experimental data, the second-order MEP distribution and the distribution measured in the long recording data indeed agree very well with each other, whereas the probability distribution measured from the short-time recording deviates significantly from them and cannot capture many neuronal activity states.

II. METHODS: THE MEP ANALYSIS

In this section, we will introduce the MEP analysis, which has been applied to estimating the probability distribution of network states for many network systems [1,2,9,30,31]. The process of performing the MEP analysis is as follows. Let $\sigma \in \{0, 1\}$ denote the state of a node in a sampling time bin, where 1 refers to an active state and 0 an inactive state. Then the state of a network of n nodes in a sampling time bin is denoted as $\Omega = (\sigma_1, \sigma_2, \ldots, \sigma_n) \in \{0, 1\}^n$. In principle, to obtain the probability distribution of Ω, one has to measure all possible states of Ω, i.e., 2^n states in total. For the case of a network of n neurons, σ often represents whether a single neuron fires in a sampling time bin in the network, where 1 corresponds to a neuron that is firing and 0 corresponds to a neuron in the silent state. We choose a typical bin size of 10 ms for the MEP analysis [2,9]. The state, Ω, in the neuronal network would represent the firing pattern of all neurons in the network.

The first-order moment of the state of node i, σ_i, is given by

$$\langle \sigma_i \rangle = \sum_{\Omega} P(\Omega) \sigma_i(\Omega), \qquad (1)$$

where $P(\Omega)$ is the probability of observing the firing pattern Ω in the recording and $\sigma_i(\Omega)$ denotes the state of the ith node in the firing pattern Ω. The second-order moment of the state of node i, σ_i, and node j, σ_j, is given by

$$\langle \sigma_i \sigma_j \rangle = \sum_{\Omega} P(\Omega) \sigma_i(\Omega) \sigma_j(\Omega), \qquad (2)$$

with higher-order moments obtained similarly. Note that, in Eqs. (1) and (2), $P(\Omega)$ can be the true probability distribution of Ω, in which case one computes the true moments; or $P(\Omega)$ can be an *observed* distribution of a finite-time recording, in which case one then estimates the moments.

The Shannon entropy of a probability distribution $P(\Omega)$ is defined as

$$S = -\sum_{\Omega} P(\Omega) \log P(\Omega). \qquad (3)$$

By maximizing this entropy, S, subject to all moments up to the mth order ($m \leqslant n$), one obtains the mth-*order MEP distribution* for a network of n nodes [1,2,9]. Note that the kth-order moments consist of all the expectations of the product of any k nodes' states [e.g., the second-order moments by Eq. (2) above for any pair of i and j with $i \neq j$] and thus when considering the constraint of the kth-order moments, there are C_n^k (the number of combinations of k nodes from n possible choices) number of constraints of kth-order moments being considered. Finally, the mth-order probability distribution is obtained from the following equation,

$$P_m(\Omega) = \frac{1}{Z} \exp\left(\sum_{k=1}^{m} \sum_{i_1 < \cdots < i_k}^{n} J_{i_1 \cdots i_k} \sigma_{i_1} \cdots \sigma_{i_k} \right), \qquad (4)$$

where, following the terminology of statistical physics, $J_{i_1 \cdots i_k}$ is called the kth-order effective interaction ($2 \leqslant k \leqslant m$), i.e., the Lagrange multiplier corresponding to the constraint of the kth-order moment $\langle \sigma_{i_1} \cdots \sigma_{i_k} \rangle$, and the partition function, Z, is a normalization factor. Equation (4) is referred to as the mth-*order MEP distribution*. In practice, we utilize a widely used iterative scaling algorithm (see Appendix A for details) to numerically solve the above MEP optimization problem to obtain the effective interactions and thus the probability distribution in Eq. (4). Here, for a network of size n, $P_n(\Omega)$ is referred to as the *full-order MEP distribution* subject to moments of all orders.

III. RESULTS

The results are organized as follows. We begin by demonstrating that there is a wide range of neuronal dynamical regimes for Hodgkin-Huxley neuronal network dynamics. Then we show that the probability distribution of network states measured from a short-time recording (data recorded from the HH network dynamics with short simulation time) cannot capture many network activity states because of large fluctuations in the measurement induced by insufficient sampling and thus differs from the probability distribution of network states measured from a long-time recording. Note that we have verified that the HH network dynamics in a long simulation time of 1.2×10^5 s reaches the steady state; therefore, the probability distribution
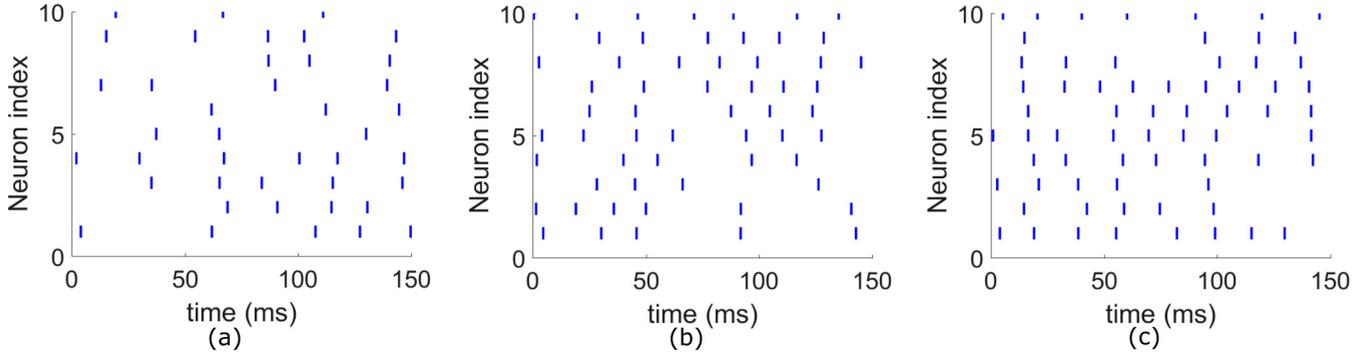
FIG. 1. Raster plots for the HH neuronal network in three different dynamical regimes. Raster plots of 10 randomly selected neurons for each case are shown. For (a), (b), and (c), consider the statistics of the interspike interval for each neuron; the Fano factor is 14.8 ± 2.9, 10.3 ± 2.3, and 4.8 ± 1, respectively, and the coefficient of variation is 0.63 ± 0.05, 0.58 ± 0.05, and 0.47 ± 0.04, respectively (mean $\pm$ std across all neurons). A short bar indicates that the neuron with certain index fires at certain time. The coupling strength is selected at random from the uniform distribution of the interval $[0, s]$, where $s = 0.071 \, \text{ms}^{-1}$ (the corresponding physiological excitatory postsynaptic potential is $\sim 1 \, \text{mV}$). The Poisson input parameters for in (a), (b), and (c) are ($\mu = 0.6 \, \text{ms}^{-1}$, $f = 0.05 \, \text{ms}^{-1}$), ($\mu = 1.1 \, \text{ms}^{-1}$, $f = 0.04 \, \text{ms}^{-1}$) and ($\mu = 2.5 \, \text{ms}^{-1}$, $f = 0.03 \, \text{ms}^{-1}$), respectively.

of network states measured from this long recording can well represent the true probability distribution of network states.

We next show that there exists a one-to-one mapping between the probability distribution of network states and the corresponding moments of the network. Then, we combine this mapping with the full-order MEP distribution to show that there exists a one-to-one mapping between all effective interactions and the probability distribution of network states. Using these mappings, we further demonstrate that high-order effective interactions are often small; thus, to accurately estimate the probability distribution of network states, one may only require accurate estimation of the low-order effective interactions. Finally, we make use of low-order moments measured in short-time recordings to estimate low-order effective interactions and show that the obtained probability distribution from the low-order MEP analysis agrees well with the probability distribution of network states. This is demonstrated by both numerical simulations of HH neuronal network dynamics and also electrophysiological experiments.

A. Short-time recordings cannot represent all network states

In this section, we first use numerical simulation data from the HH neuronal network dynamics and show that short-time recordings are often insufficient to accurately estimate the probability distribution of network states. Later, we will also demonstrate this issue using experimental data from electrophysiological measurements.

We simulate a network of 80 excitatory and 20 inhibitory HH neurons, with a 20% connection density among neurons in the network. As physiological experiments can often only measure a subset of neurons, we randomly select 10% of the neurons in the network (10 neurons) and demonstrate differences in the directly measured probability distribution between the short and the long recording. Note that there are typically three dynamical regimes for neuronal networks [32]: (i) a highly fluctuating regime where the input rate, μ, is low [Fig. 1(a)]; (ii) an intermediate regime where μ is moderately

high [Fig. 1(b)]; and (iii) a low fluctuating or mean-driven regime where μ is very high [Fig. 1(c)]. We evolve the HH neuronal network dynamics and record the spike trains of all neurons for a duration of 1.2×10^5 s, which is sufficiently long to obtain a stable probability distribution of neuronal firing patterns. We then compare the probability distribution of network states directly measured in the short-time recording of 120 s to that measured in the long recording. As shown in Fig. 2, the measured probability distribution of firing patterns in the short-time recording deviates substantially from that in the long recording for all three dynamical regimes.

The probability distribution of network states is important for a complete understanding of the underlying function of networks [4,5] despite the fact that a sufficient long-time data recording is often impossible or impractical. Thus, it is essential to obtain an accurate estimate of the probability distribution of network states from a short-time recording. To achieve this, we next study relationships among the probability distribution, the moments, and the effective interactions in the MEP distribution and show that the second-order MEP analysis often gives rise to an accurate estimate of the probability distribution of network states.

B. One-to-one mapping between the probability distribution and the moments

To demonstrate the relationship between the true probability distribution of network states, $P_{\text{true}}(\Omega)$, and the corresponding moments, we introduce several notations for ease of discussion. First, denote the vector $\mathbf{P}^{(n)} = [p_1^{(n)}, p_2^{(n)}, \ldots, p_{2^n}^{(n)}]^T$ as the vector containing the probability distribution of the network states for a network of n nodes, and denote the vector $\mathbf{M}^{(n)} = [m_1^{(n)}, m_2^{(n)}, \ldots, m_{2^n}^{(n)}]^T$ as the vector containing all moments of the network. We arrange the entries in $\mathbf{P}^{(n)}$ and $\mathbf{M}^{(n)}$ as follows. For an example network of size $n = 2$, we assign values to the ith entry by expressing $i - 1$ using the base-2 number system with total $n = 2$ digits, i.e., $E_i = e_2 e_1$, where E_i represents the combined state of the two nodes in the network, e_1 and e_2 (e.g., 00 corresponds to
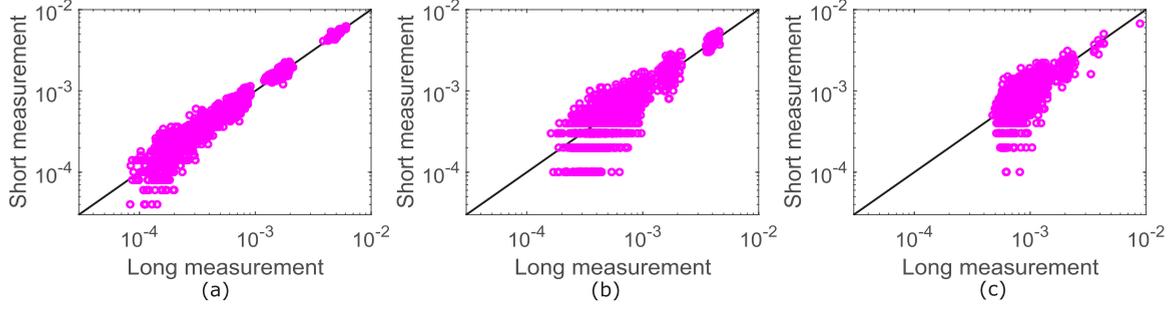
FIG. 2. Measured probability distributions for short-time recordings compared with long-time recordings. The frequency of each firing state measured from the short-time recording of network dynamics (120 s) is plotted against the frequency measured from the long-time recording of network dynamics (1.2×10^5 s). Data for these three cases are from three dynamical regimes shown (the same 10 selected neurons in each case) in Fig. 1, respectively.

both nodes being inactive), as shown in the second column of Table I. Then, for each i, denote the probability of the network state ($\sigma_1 = e_1$, $\sigma_2 = e_2$) as $p_i^{(2)}$, as shown in the third column of Table I. In neuroscience, the vector P_{00} represents the probability of finding both two neurons in the quiet state, P_{10} (P_{01}) represents the probability of the first (second) neuron in the active state and the second (first) neuron in the silent state, and P_{11} represents the probability of both neurons in the active state. The entries in the vector $\mathbf{M}^{(2)}$ are arranged similarly, i.e., $m_i^{(2)}$ is the expectation of $(\sigma_1)^{e_1}(\sigma_2)^{e_2}$, as shown in the fourth column of Table I.

For illustration, we show that, for a network of $n = 2$ nodes, there is a full-rank matrix, $\mathbf{U}_{PM}^{(2)}$, that transforms from the probability distribution to moments. From Eqs. (1) and (2), the expectation of σ_1, σ_2, and $\sigma_1\sigma_2$ can be obtained by summing the probabilities in which those nodes are active, leading to the following system:

$$\begin{bmatrix} 1 & 1 & 1 & 1 \\ 0 & 1 & 0 & 1 \\ 0 & 0 & 1 & 1 \\ 0 & 0 & 0 & 1 \end{bmatrix} \begin{bmatrix} P_{00} \\ P_{10} \\ P_{01} \\ P_{11} \end{bmatrix} = \begin{bmatrix} 1 \\ \langle\sigma_1\rangle \\ \langle\sigma_2\rangle \\ \langle\sigma_1\sigma_2\rangle \end{bmatrix}, \qquad (5)$$

i.e., $\mathbf{U}_{PM}^{(2)}\mathbf{P}^{(2)} = \mathbf{M}^{(2)}$. Clearly, from Eq. (5), $\mathbf{U}_{PM}^{(2)}$ is upper triangular and of full rank.

The above analysis can be extended to a network of any size n. For each integer i, $1 \leqslant i \leqslant 2^n$, we can similarly express $i - 1$ by the base-2 number system with n digits, denoted by $E_i = e_n e_{n-1} \cdots e_2 e_1$. Then write the probability of the network state ($\sigma_1 = e_1$, $\sigma_2 = e_2, \ldots, \sigma_n = e_n$), denoted as $p_i^{(n)}$, and the moment, i.e., the expectation of $(\sigma_1)^{e_1}(\sigma_2)^{e_2} \cdots (\sigma_{n-1})^{e_{n-1}}(\sigma_n)^{e_n}$, denoted as $m_i^{(n)}$, as follows:

$$\mathbf{P}^{(n)} = \begin{bmatrix} P_{00\cdots0} \\ P_{10\cdots0} \\ P_{01\cdots0} \\ P_{11\cdots0} \\ \vdots \\ P_{01\cdots1} \\ P_{11\cdots1} \end{bmatrix}, \quad \mathbf{M}^{(n)} = \begin{bmatrix} 1 \\ \langle\sigma_1\rangle \\ \langle\sigma_2\rangle \\ \langle\sigma_1\sigma_2\rangle \\ \vdots \\ \left\langle\prod_{j=2}^n \sigma_j\right\rangle \\ \left\langle\sigma_1\prod_{j=2}^n \sigma_j\right\rangle \end{bmatrix}. \quad (6)$$

We prove that there is a full-rank matrix, $\mathbf{U}_{PM}^{(n)}$, that transforms from $\mathbf{P}^{(n)}$ to $\mathbf{M}^{(n)}$ as

$$\mathbf{U}_{PM}^{(n)}\mathbf{P}^{(n)} = \mathbf{M}^{(n)}, \qquad (7)$$

where $\mathbf{U}_{PM}^{(n)}$ is upper triangular and of full rank (see Appendix C for details).

Therefore, all moments, which are shown in the entries of $\mathbf{M}^{(n)}$, can be used to describe the probability distribution of network states for a network of n nodes with binary dynamics. As the full-order MEP distribution, $P_n(\Omega)$, is subject to all moments, $P_n(\Omega)$ and $P_{\text{true}}(\Omega)$ share the same moments for a sufficiently long-time recording, i.e., $\mathbf{M}^{(n)}$ in Eq. (7). Since $\mathbf{U}_{PM}^{(n)}$ is of full rank, $P_n(\Omega)$ is identical to $P_{\text{true}}(\Omega)$.

By directly substituting $P_{\text{true}}(\Omega)$ into the full-order MEP analysis, we develop a relationship between effective interactions and the probability distribution, as discussed in the next section.

C. One-to-one mapping between effective interactions and the probability distribution

To demonstrate the relationship between effective interactions and the true probability distribution of network states, we substitute all 2^n states of $\Omega = (\sigma_1, \sigma_2, \ldots, \sigma_n)$ and the probability distribution, $P_{\text{true}}(\Omega)$, into Eq. (4) with $m = n$ and then take the logarithm of both sides. This results in a system of linear equations in terms of $-\log Z$ and all the effective interactions,

$$-\log Z + \sum_{k=1}^n \sum_{i_1 < \cdots < i_k}^n J_{i_1 \cdots i_k}\sigma_{i_1}\cdots\sigma_{i_k} = \log P_{\text{true}}(\Omega), \quad (8)$$

where $-\log Z$ can be regarded as the zeroth-order effective interaction, J_0. By solving the system of linear equations in

TABLE I. Table of entries for building the vectors $\mathbf{P}^{(n)}$ and $\mathbf{M}^{(n)}$ for an example network of $n = 2$ nodes.

i	$E_i = e_2 e_1$	$p_i^{(2)}$	$m_i^{(2)}$
1	00	P_{00}	1
2	01	P_{10}	$\langle\sigma_1\rangle$
3	10	P_{01}	$\langle\sigma_2\rangle$
4	11	P_{11}	$\langle\sigma_1\sigma_2\rangle$

Eq. (8), we can obtain all the 2^n effective interactions, J's, in terms of the true probability distribution of network states, $P_{\text{true}}(\Omega)$.

We again turn to the small network case of $n = 2$ nodes to demonstrate how to obtain a one-to-one mapping from the linear system described by Eq. (8). First, denote the vector $\mathbf{J}^{(2)}$ as the vector containing all the effective interactions, with the index of each effective interaction, i. We then express $i-1$ by the base-2 number system with total $n = 2$ digits, denoted by $E_i = e_2 e_1$, and the ith entry of $\mathbf{J}^{(2)}$ is the coefficient of the term $(\sigma_1)^{e_1}(\sigma_2)^{e_2}$ in Eq. (8), yielding $\mathbf{J}^{(2)} = (J_0, J_1, J_2, J_{12})^T$. Since the ordering of the indices for $\mathbf{J}^{(2)}$ is the same as that of $\mathbf{P}^{(2)}$, then the right-hand side of Eq. (8) is simply the logarithm of the vector $\mathbf{P}^{(2)}$. Therefore, for a network of $n = 2$ nodes, we have the following equation:

$$\begin{bmatrix} 1 & 0 & 0 & 0 \\ 1 & 1 & 0 & 0 \\ 1 & 0 & 1 & 0 \\ 1 & 1 & 1 & 1 \end{bmatrix} \begin{bmatrix} J_0 \\ J_1 \\ J_2 \\ J_{12} \end{bmatrix} = \begin{bmatrix} \log P_{00} \\ \log P_{10} \\ \log P_{01} \\ \log P_{11} \end{bmatrix}. \tag{9}$$

The above relation can be extended to a network of any size n and the corresponding linear equations are as follows:

$$\mathbf{L}_{\text{JP}}^{(n)} \mathbf{J}^{(n)} = \log \mathbf{P}^{(n)}, \tag{10}$$

where $\mathbf{L}_{\text{JP}}^{(n)}$ is a lower-triangular matrix with dimension $2^n \times 2^n$. For $1 \leqslant i \leqslant 2^n$, we can similarly express $i-1$ by the base-2 number system with n digits, denoted by $E_i = e_n e_{n-1} \cdots e_2 e_1$. Then, the ith entry of $\mathbf{J}^{(n)}$ is the coefficient of the term $(\sigma_1)^{e_1}(\sigma_2)^{e_2} \cdots (\sigma_{n-1})^{e_{n-1}}(\sigma_n)^{e_n}$ in Eq. (8). To show the linear transform between the effective interactions in the full-order MEP distribution $\mathbf{J}^{(n)}$ and the probability distribution of network states $\mathbf{P}^{(n)}$ is a one-to-one mapping, one needs to demonstrate that $\mathbf{L}_{\text{JP}}^{(n)}$ is a matrix of full rank. Similarly, as the proof of the one-to-one mapping between the probability distribution and the moments, we can show that $\mathbf{L}_{\text{JP}}^{(n)}$ is the transpose of $\mathbf{U}_{\text{PM}}^{(n)}$, i.e., $\mathbf{L}_{\text{JP}}^{(n)} = [\mathbf{U}_{\text{PM}}^{(n)}]^T$ by mathematical induction. Therefore, $\mathbf{L}_{\text{JP}}^{(n)}$ is lower triangular and full-rank, and one can use effective interactions to characterize the probability distribution of network states for a network of nodes with binary dynamics.

Note that the transformations among probability, moment, and effective interaction have been studied previously [33–35]. Our focus here is to point out that the matrices $\mathbf{U}_{\text{PM}}^{(n)}$ and $\mathbf{L}_{\text{JP}}^{(n)}$ are upper and lower triangular, respectively. The triangular property of the matrices indicates that a lower-order moment is a summation including probability of network states that occur frequently, which facilitates a better estimation for the lower-order moment. In addition, a recursive relation among different-order effective interactions can be directly obtained from $\mathbf{L}_{\text{JP}}^{(n)}$ (see Appendix E), which is useful for the analysis in the section below.

D. High-order effective interactions are often small

To provide an understanding to the fact that high-order effective interactions are often small, we show a recursive relation among different-order effective interactions based on the one-to-one mapping (see Appendix E). Compared with the general expression of effective interactions in other studies

[33,36], this recursive relation indicates that high-order effective interactions can be expressed as increments of low-order effective interactions induced by the state change of individual neurons.

For illustration, we first discuss the case of a network with size $n = 2$. Based on Eq. (9), we have

$$J_0 = \log P_{00}, \quad J_1 = \log \frac{P_{10}}{P_{00}}, \quad J_2 = \log \frac{P_{01}}{P_{00}},$$

and

$$J_{12} = \log \frac{P_{11}}{P_{01}} - \log \frac{P_{10}}{P_{00}}.$$

Next, we define a new term,

$$J_1^1 \triangleq \log \frac{P_{11}}{P_{01}},$$

which describes the case in which the state of the second node in the network is changed from inactive (state 0) to active (state 1) (i.e., in J_1, $P_{10} \to P_{11}$, and $P_{00} \to P_{01}$). Note that with this notation, we can now express the higher-order effective interaction, J_{12}, as

$$J_{12} = J_1^1 - J_1.$$

For a network of any size n, based on Eq. (10), we obtain an expression for the first-order effective interaction

$$J_1 = \log \frac{P_{10\cdots0}}{P_{00\cdots0}} \tag{11}$$

and for the second-order effective interaction

$$J_{12} = \log \frac{P_{110\cdots0}}{P_{010\cdots0}} - \log \frac{P_{10\cdots0}}{P_{00\cdots0}}. \tag{12}$$

Then, the second-order effective interaction, J_{12}, can be equivalently obtained by the following procedure: First, in $J_1 = \log(P_{10\cdots0}/P_{00\cdots0})$, we switch the state of the second node from 0 to 1 to obtain a new term $J_1^1 = \log(P_{110\cdots0}/P_{010\cdots0})$. Then, note that if we subtract J_1 from J_1^1, then we arrive at J_{12} as described in Eq. (12). As shown in Appendix E, with the one-to-one mapping, the above notation can be extended to the case of high-order effective interactions (or see Appendix D for a general proof):

$$J_{12\cdots(k+1)} = J_{12\cdots k}^1 - J_{12\cdots k}, \tag{13}$$

where $1 \leqslant k \leqslant n - 1$ and $J_{12\cdots k}^1$ is obtained by switching the state of the $(k+1)$st node in $J_{12\cdots k}$ from 0 to 1. We refer to this recursive relation as *J-relation*. Next, we intuitively explain that the J-relation [Eq. (13)] leads to the hierarchy of effective interactions, i.e., high-order effective interactions are often much smaller than low-order ones. $J_{12\cdots k}$ describes the effective interaction of the subnetwork of neurons $\{1, 2, 3, \ldots, k\}$ when the state of the $(k+1)$st neuron and states of neurons with indices $\{k+2, k+3, \ldots, n\}$ are inactive. The term $J_{12\cdots k}^1$ describes the case in which the $(k+1)$st neuron becomes active and states of all other neurons are not changed. Therefore, compared with the general expression of effective interactions in other studies [33,36], this recursive relation reveals that high-order effective interactions can be understood as increments of low-order effective interactions. In many neuronal networks, the influence on the whole network induced by the

state change of an individual neuron is often small. In other words, the value difference between the effective interaction of the subnetwork where the $(k + 1)$st neuron is inactive, $J_{12\cdots k}$, and the effective interaction when the $(k + 1)$st neuron is active, $J_{12\cdots k}^1$, should be small, and thus the higher-order effective interaction, $J_{12\cdots(k+1)}$, is often much smaller than the low-order effective interaction, $J_{12\cdots k}$. Note that more strict mathematical proof of the hierarchy of effective interactions can be seen in our previous work [3]. Therefore, the J-relation in Eq. (13) leads to a hierarchy of effective interactions, i.e., low-order effective interactions dominate higher-order effective interactions in the MEP analysis.

Note that the solution of Eq. (10) was used in Ref. [19] to obtain the approximate effective interactions in the MEP analysis. As criticized by Ref. [29], the final estimated distribution in Ref. [19] is not a normalized probability distribution. Here we focus more on the inner structure of the solution of Eq. (10) to obtain the J-relation in Eq. (13). We use this relation to rationalize that most high-order effective interactions are often small, but do not use it for direct estimation of effective interactions as in Ref. [19].

Next we investigate the HH neuronal network dynamics to confirm that the first two-order effective interactions in the full-order MEP distribution dominate higher-order effective interactions. We evolve HH networks in a long-time simulation of 1.2×10^5 s and measure the probability distribution of network states. We have verified that the HH network dynamics in such a long simulation time reaches the steady state, and, therefore, the measured probability distribution of network states can well represent the true probability distribution of network states. We then calculate effective interactions in the full-order MEP distribution by Eq. (10) from the measured probability distribution of network states. In the first row of Fig. 3, the average strength of the kth-order effective interactions is computed as the mean of the absolute value of the kth-order effective interactions. It can clearly be seen that for three different dynamical regimes, the average strength of effective interactions of high-orders ($\geqslant 3$) are at least one order of magnitude smaller (in the absolute value) than that of the first-order and the second-order effective interactions. The number of high-order effective interaction can overwhelm the number of low-order ones. To show that high-order effective interactions do not accumulate to produce a significant effect on the characterization of the probability distribution of network states, we compute the summation of all same-order effective interactions. As shown in the second row of Fig. 3, we found that the low-order effective interactions still dominate high-order effective interactions.

E. Low-order MEP analysis with short-time recordings

Using the mappings described in the previous sections, we show that the low-order MEP analysis can provide an accurate estimate of the probability distribution of network states with a short-time recording.

First, note that in a short-time recording, the network states with small probability usually cannot be measured accurately (e.g., shown in Fig. 2). The mapping between the probability distribution and effective interactions, i.e., the lower-triangular matrix $\mathbf{L}_{JP}^{(n)}$, suggests that the probability

of a network state consists of the summation of effective interactions with indices concerning those active nodes. For example, in a small network of $n = 2$ nodes, $P(\sigma_1 = 1, \sigma_2 = 1)$ can be obtained from Eq. (9) by $\log P_{11} = J_0 + J_1 + J_2 + J_{12}$. Therefore, to obtain an accurate probability estimation of network states, it is important to obtain an accurate estimation of the summation of the effective interactions.

For many neuronal networks, since high-order effective interactions are often small (e.g., shown in Fig. 3), the summation in the probability of a network state will be dominated by low-order effective interactions. Note that low-order effective interactions can be derived from low-order moments through a commonly used iterative scaling algorithm (see Appendix A for details) in the MEP analysis, and thus an accurate estimation of low-order moments is essential. The mapping between the probability distribution of network states and corresponding moments of the network, i.e., the upper-triangular matrix $\mathbf{U}_{PM}^{(n)}$ [Eq. (5)], shows that low-order moments consist of the summation of probabilities of many network activity states. For example, in a network of n nodes, the first-order moment of node 1 is the summation of network state probabilities where node 1 is active (2^{n-1} states in total), that is, $\langle \sigma_1 \rangle = P_{10\cdots0} + P_{11\cdots0} + \cdots + P_{11\cdots1}$. The estimation error in low-order moments can be reduced due to linear summations of many terms regarding network state probabilities. Therefore, one can accurately estimate the low-order moments and perform the low-order MEP analysis in a short-time data recording of network dynamics. It is expected that the low-order MEP distribution provides a good estimate of the probability distribution of network states.

In summary, the low-order MEP distribution can be obtained by the following procedure: First, calculate low-order moments from the experimental short-time recording using Eqs. (1) and (2) for the first-order and the second-order moments, respectively. Second, the low-order MEP analysis (with constraints of low-order moments) is carried out using the widely used iterative scaling algorithm (see Appendix A for details) to derive the low-order effective interactions with all higher-order effective interactions set to zero. This determines $\mathbf{J}^{(n)}$ in Eq. (10), except for J_0. Third, express the probability distribution, $\mathbf{P}^{(n)}$, as a function of J_0 using Eq. (10). Finally, determine J_0 by constraining the summation of all probabilities to equal 1. Once all the low-order effective interactions are determined, Eq (4) is used to determine the low-order MEP distribution, e.g., $P_1(\Omega)$ and $P_2(\Omega)$ represents for the first-order and the second-order MEP distribution, respectively.

F. Verification for the MEP analysis with short-time recordings by HH neuronal network model

In this section, we use data from the HH neuronal network model to verify that low-order MEP analysis can accurately estimate the probability distribution of network states from short-time recordings using the procedure described in the previous section.

We first evolve the HH neuronal network model with a short simulation time of 120 s and record the spike trains of the network. Then we estimate the first-order and the second-order moments from this short-time recording and
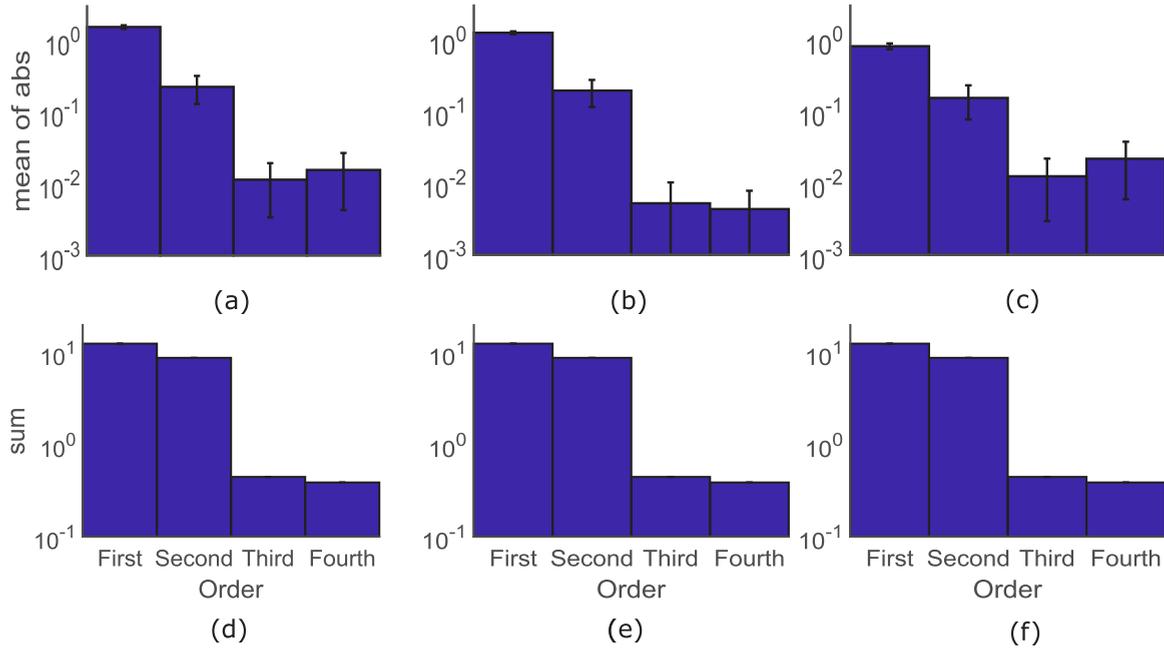
FIG. 3. Hierarchy of effective interactions in the MEP analysis in three dynamical regimes. In the first row, mean absolute values of effective interactions from the first order to the fourth order for three different dynamical regimes (shown in Fig. 1) are plotted, with the standard deviation indicated by the error bar. In the second row, the absolute value of the summation of all same-order effective interactions from the first order to the fourth order is plotted. Data for these three cases are collected from the three experiments (the same 10 selected neurons in each case) in Fig. 1, respectively, with a long recording time of 1.2×10^5 s.

use these two-order moments to estimate both the first-order and the second-order MEP distributions [Eq. (4)]. Finally, we compare the MEP distributions to the probability distribution of network states measured from the long recording of 1.2×10^5 s. As shown in Fig. 4, for all three dynamical regimes, the probability distribution of the first-order MEP analysis, P_1 (green), deviates substantially from the measured probability distribution of network states in the long recording. The probability distribution of the second-order MEP analysis, P_2 (blue), however, is in excellent agreement with the measured probability distribution of network states in the long recording.

Next, we use Kullback-Leibler (KL) divergence to quantify the distance between the probability distribution measured from the long recording (denoted by P_{true}) and the one estimated by the second-order MEP analysis based on a short-time recording (denoted by P_2), that is,

$$D(P_{\text{true}}, P_2) = \sum_{\Omega} P_{\text{true}}(\Omega) \log P_{\text{true}}(\Omega)/P_2(\Omega).$$

Similarly, $D(P_{\text{true}}, P_{\text{short}})$ can be defined, where P_{short} stands for the probability distribution directly measured from the short-time recording. As shown in the second row of Fig. 4, the KL divergence decreases following an approximate power law as the recording length increases. This indicates the KL divergence decreases very fast at the beginning and then very slowly at latter stages. In addition, $D(P_{\text{true}}, P_{\text{short}})$ is always one order of magnitude larger than $D(P_{\text{true}}, P_2)$ across different dynamical regimes. These results indicate that the low-order, i.e., second-order, MEP analysis provides an efficient

method to obtain the probability distribution of network states with short-time recordings.

G. Verification for the MEP analysis with short-time recordings by electrophysiological experiments

In general, it is difficult to obtain a stationary long-time recording of spike trains from the brain of an awake animal *in vivo*. To verify the validity of the MEP analysis on short-time recordings, we use the electrophysiological experimental data recorded by multielectrode array from V1 in *anesthetized* macaque monkeys in multiple trials. For each trial, an image stimulus was shown on the screen for 100 ms, followed by a 200-ms uniform gray screen [37,38]. The number of different images is 956 in total and images are presented in pseudorandom order with each presented 20 times. Experimental details can be found in Appendix F. Here we focus on the issue of whether the second-order MEP analysis from a short-time recording can accurately estimate the probability distribution of neuronal firing patterns in a long recording. Note that the presenting duration for each image is only 2 s, which is too short for the recorded spike trains to have a stable probability distribution. As an alternative, we put the spike trains recorded during the uniform gray screen (200 ms in each trial) altogether to obtain a long recording of 3824 s. We have verified that the spike trains in such a long recording has a stable probability distribution. For a short-time recording, we randomly select 5% length of the long recording, i.e., 191.2 s, and also verified that the probability distribution in such a short-time recording is quite different from that in the long recording. To perform the MEP analysis, we randomly
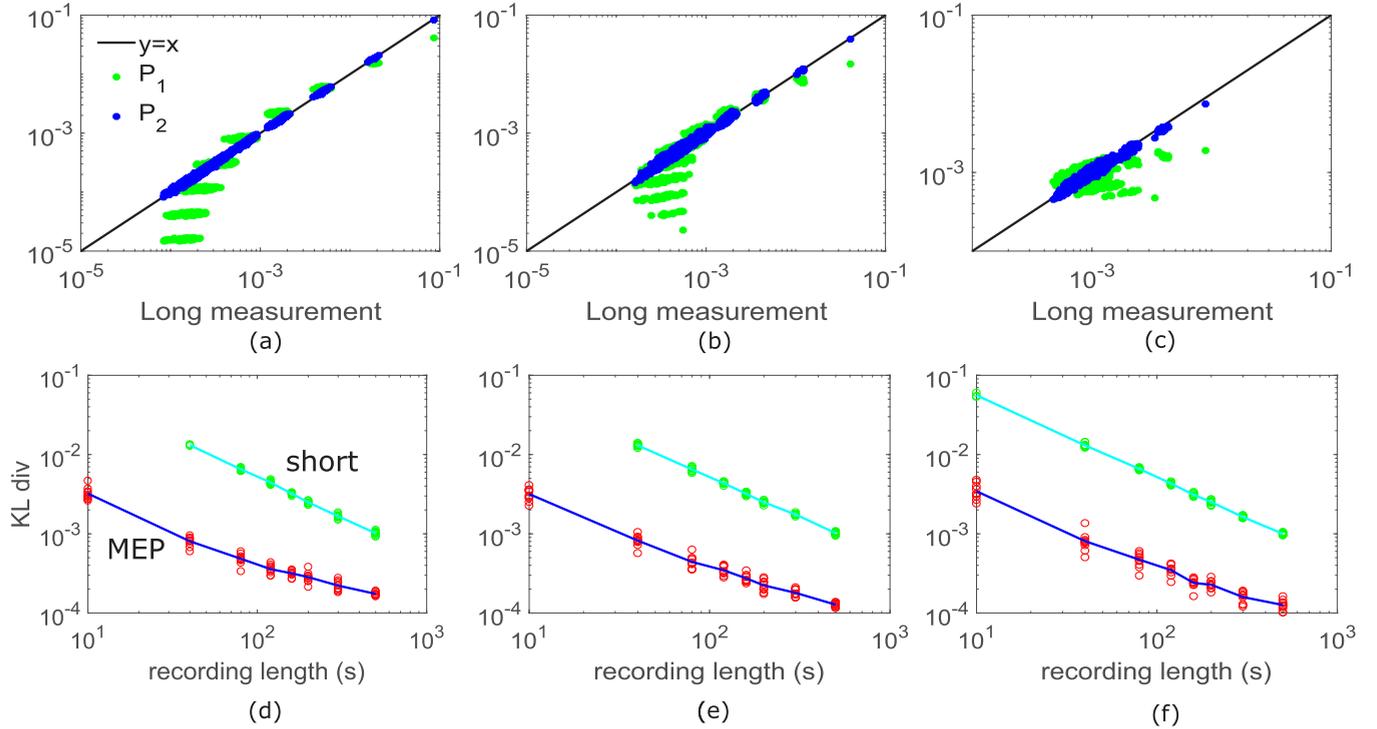
FIG. 4. First-order and second-order MEP distribution in comparison with the probability distribution of network states. In the first row, the frequency of each firing state from the distribution of the MEP analysis, P_2 (blue) and P_1 (green), is plotted against the frequency measured from the long recording (1.2×10^5 s). Data for three different dynamical regimes (shown in Fig. 1) are collected from the three experiments (the same 10 selected neurons in each case) in Fig. 1, respectively. Here the MEP analysis is performed with a short-time recording (1.2×10^2 s). In the second row, for each dynamical regime, each red circle is one trial of $D(P_{\text{true}}, P_2)$ against the short-recording length. The blue line is the mean of 10 trials for each recording length. The green circles and the cyan line are for the distribution directly measured from the short-time recording, i.e., $D(P_{\text{true}}, P_{\text{short}})$. Some circles are missing because the KL divergence cannot be computed due to some firing patterns (zero probability in the measurement) not present in the short-time recording.

selected eight neurons' spike train data from experimental measurements. The raster plot of these eight neurons are shown in Fig. 5(a).

We then calculate effective interactions in the full-order MEP distribution by Eq. (10) using the measured probability distribution of network states from the long recording of 3824 s. In Fig. 5(b), the average strength of the kth-order effective interactions is computed as the mean of the absolute value of the kth-order effective interactions. It can be seen clearly that the average strength of effective interactions of high orders ($\geqslant 3$) are almost one order of magnitude smaller (in the absolute value) than that of the first-order and the second-order effective interactions. To show that high-order effective interactions do not accumulate to produce a significant effect in the characterization of the probability distribution of network states, we compute the summation of all same-order effective interactions. As shown in Fig. 5(c), we found that the low-order effective interactions still dominate high-order effective interactions. Next, we consider a short-time recording of 191.2 s and estimate the first-order and the second-order moments from this short-time recording and use these moments to estimate the second-order MEP distributions [Eq. (4)]. As shown in Fig. 5(d), the probability distribution estimated by the second-order MEP analysis is in excellent agreement with the measured probability distribution of network states in the long recording. However, the

probability distribution measured in the short-time recording clearly deviates from the probability distribution measured in the long recording.

Next, we similarly use KL divergence to quantify the distance between probability distributions. When the recording length is short, $D(P_{\text{true}}, P_{\text{short}})$ often cannot be computed due to some firing patterns (zero probability in the measurement) not present in the short-time recording. Here we use an approximate KL divergence for such cases, that is, we only consider states observed in the short-time recording,

$$D_{\text{approx}}(P_{\text{true}}, P_{\text{short}})$$
$$= \sum_{\Omega:P_{\text{short}}(\Omega)>0} P_{\text{true}}(\Omega) \log P_{\text{true}}(\Omega)/P_{\text{short}}(\Omega).$$

As shown in Fig. 5(e), when the recording length is less than 400 s, the second-order MEP distribution based on the short-time recording, P_2, is more accurate than the one directly measured from the short-time recording, P_{short}. When the recording time is larger than 400 s, P_{short} becomes closer to P_{true} than P_2. Since high-order effective interactions do not totally vanish, the accuracy of P_2 will saturate when the recording time gets long, while the accuracy of P_{short} can keep increasing as the recording time increases. The impact of high-order effective interactions on the insufficiency of the second-order MEP analysis is also consistent with previous
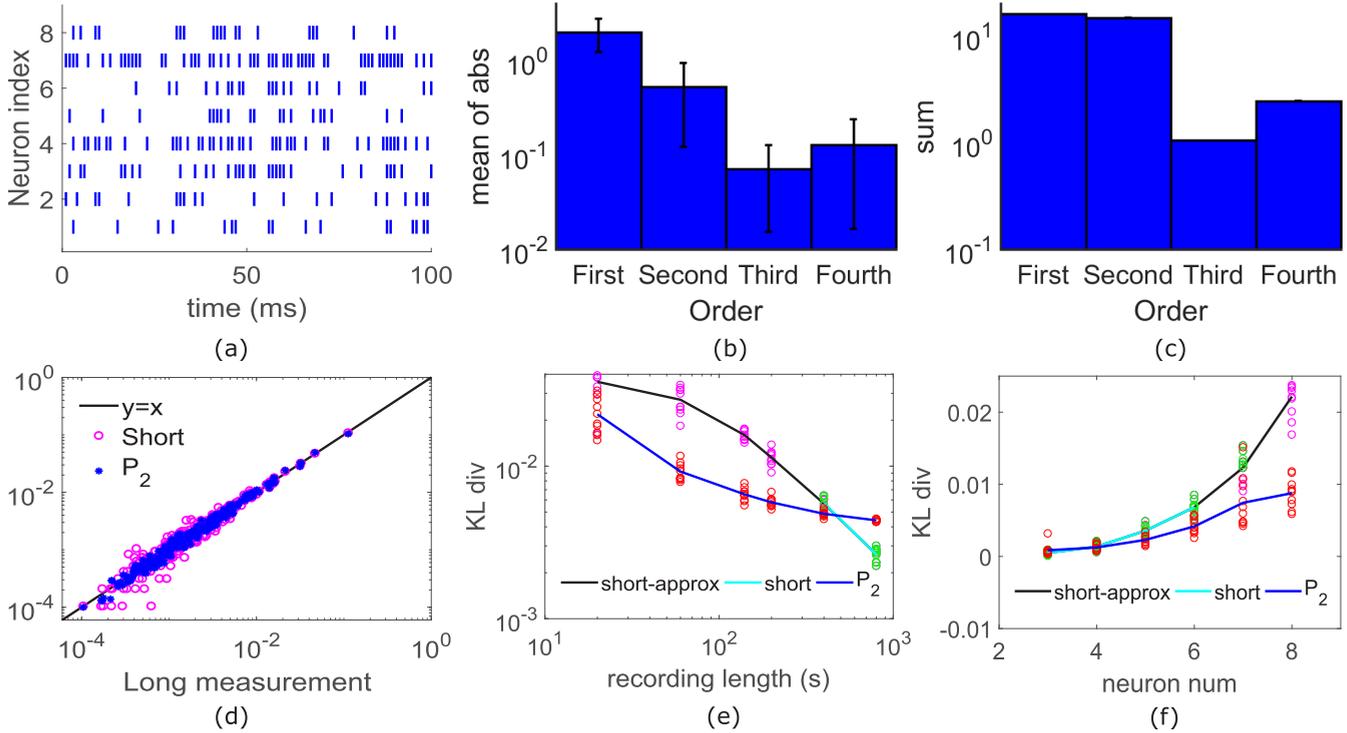
FIG. 5. Electrophysiological verification for the second-order MEP analysis with short-time recordings. Spike trains of randomly selected eight neurons are recorded from V1 in *anesthetized* macaque monkeys (see Appendix F). (a) A short bar indicates that the neuron with certain index fires at certain time. The Fano factor and the coefficient of variation for the interspike interval is 6.1 ± 2.8 and 1.3 ± 0.2, respectively (mean $\pm$ std across all neurons). (b) Mean absolute values of effective interactions from the first order to the fourth order are plotted, with the standard deviation indicated by the error bar, computed by the long recording of 3824 s. (c) The absolute value of the summation of all same-order effective interactions from the first order to the fourth order is plotted, computed by the long recording of 3824 s. (d) The frequency of each firing state from the distribution measured in the short-time recording of 191.2 s (magenta) and the distribution of the second-order MEP analysis, P_2 (blue), is plotted against the frequency measured from the long recording of 3824 s. (e) Each red circle is one trial of $D(P_{\text{true}}, P_2)$ against the short-recording length. The blue line is the mean of 10 trials for each recording length. The green circles and the cyan line are KL divergence for the distribution directly measured from the short-time recording, i.e., $D(P_{\text{true}}, P_{\text{short}})$. Some circles are missing because the KL divergence cannot be computed due to some firing patterns (zero probability in the measurement) not present in the short-time recording. The magenta circles and the black line are approximate KL divergence for the distribution directly measured from the short-time recording, i.e., $D_{\text{approx}}(P_{\text{true}}, P_{\text{short}})$. (f) The plot is similar to (e), except that the abscissa is the number of considered neurons. In each trial, neurons are randomly selected and the recording length is 100 s.

studies [19,25,27,29]. Figure 5(e) also indicates that although there exist nonvanishing high-order effective interactions, the second-order MEP analysis is still an effective tool to characterize the probability distribution of network states for short-time recordings, e.g., dozens of seconds, compared with the direct measurement from the short-time recordings.

The above analysis can also be applied to study how the performance of the second-order MEP analysis depends on the number of considered neurons. As shown in Fig. 5(f), the KL divergence gap between $D(P_{\text{true}}, P_2)$ and $D(P_{\text{true}}, P_{\text{short}})$, or $D_{\text{approx}}(P_{\text{true}}, P_{\text{short}})$, increases significantly as the number of considered neurons increases. This indicates that for a large population of neurons, it is expected that P_2 is much more accurate than P_{short} for short-time recordings.

IV. DISCUSSION

The second-order MEP analysis has been used to infer the probability distribution of network states under various conditions, such as under spontaneous activity of neuronal networks [2,9] or visual input [1]. Since the second-order MEP distribution can be obtained by maximizing the Shannon entropy with measured constraints of only the first-order and the second-order moments, the curse of dimensionality is circumvented and an accurate estimation of the probability distribution of network states is provided. A series of works have been initiated to address various aspects of this approach, including explorations of fast algorithms [39,40], the inference of spatial-temporal correlations [9,41–44], and the characterization of network functional connectivity [45–50].

In addition to spiking neuronal networks [1], the MEP analysis has been applied to analyzing various types of binary data. These applications include, for example, functional magnetic resonance imaging data [48], in which each brain region is considered to be either active or silent, and stock market data [30], in which the price of each stock is considered to be increasing or not. However, for all these binary data, long-time recordings are often impractical to be obtained.

In this work, we begin by showing that there exist invertible linear transforms among the probability distribution of network states, the moments, and the effective interactions in the MEP analysis for a general network of nodes with binary dynamics. Based on these transforms, we show that the second-order MEP analysis gives rise to a better estimate of the probability distribution of network states with a short-time recording than the one directly measured from the short-time recording. To intuitively understand the mechanism underlying the above conclusion, one may consider the case of estimating a Gaussian distribution through a set of samples. The mean and the variance (resembling the first two-order moments) can be accurately estimated, which can determine the full distribution with the prior knowledge that the distribution is a Gaussian (resembling the second-order MEP distribution). Then the small-probability states—which are very noisy in the sampling set—can also be accurately retrieved. To verify our conclusion, we use data from both the simulated HH neuronal network model and the electrophysiological experiment to demonstrate the good performance of the second-order MEP analysis with short-time recordings. Note that the insufficiency of the second-order MEP distribution becomes significant when the recording time is long, and this is consistent with results discussed in the literature [22–26]. However, our results here show that the MEP analysis with short-time recording gives rise to a better estimation of the probability distribution of network states than the one directly measured from the short-time recording. Therefore, the applicability of the second-order MEP analysis in practical situations could be significantly improved.

Finally, we point out that there are also some limitations on low-order MEP analysis. First, low-order MEP analysis could fail to describe the probability distribution of certain network states, e.g., multiple firing events [51,52]. It requires more investigation of the short-time MEP analysis in which high-order effective interactions are important [19,29]. Second, as both the order of moment constraints and the network size, n, increase, the existing algorithms to estimate effective interactions for a large network become very slow [39,53]. Because the number of all network states, i.e., 2^n, is too large when n is a large number, the existing algorithms estimate moments of the MEP distribution using Monte Carlo sampling from the MEP distribution, which are often very slow when the dimension of the distribution is high [39,53]. Third, the impact of high-order effective interactions may become more and more significant as the number of neurons grows. As an illustration, we perform an analysis for small populations on how the strength of high-order effective interactions grows with the number of neurons. We study the absolute value of the summation of all same-order effective interactions computed from the electrophysiological data (the same procedure as that in Fig. 5). As shown in Fig. 6, the amplitude of summation of high-order effective interactions grows faster than low-order ones as the number of neurons increases. This is consistent with results in Ref. [27] that the second-order MEP analysis might not perform well in a large network of sensory neurons. Therefore, how to efficiently characterize the statistical properties of strongly correlated network dynamics and how to develop fast numerical algorithms for the application of the MEP analysis in large-scale
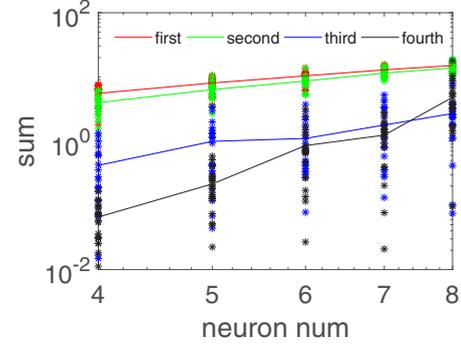

FIG. 6. The strength of summation of effective interactions vs. the number of neurons. The plot is the absolute value of the summation of all same-order effective interactions computed from the electrophysiological data (the same procedure as that in Fig. 5) for the first (red), second (green), third (blue), and fourth order (black). For each considered neuron number M, we analyze 20 different subnetworks of randomly selected M neurons from the recording data. Each star is the result of one subnetwork consisting of M neurons with different colors for different-order effective interactions. The solid line corresponds to the mean value of summation from all 20 different subnetworks consisting of M neurons.

networks remain interesting and challenging issues for future studies.

ACKNOWLEDGMENTS

APPENDIX A: THE ITERATIVE SCALING ALGORITHM

We briefly describe the widely used numerical algorithm for the estimation of effective interactions from moments. More details about this algorithm can be found in Ref. [9]. For illustration, we present the procedure to obtain the second-order MEP distribution, $P_2(\Omega)$. The interactions are initialized by $J_i = \langle \sigma_i \rangle_{P(\Omega)}$ and $J_{ij} = \langle \sigma_i \sigma_j \rangle_{P(\Omega)}$, where $\langle \cdot \rangle_{P(\Omega)}$ denotes the expectation with respect to the measured probability distribution of network states in data recording, $P(\Omega)$. The expected values of the individual means $\langle \sigma_i \rangle_{P_2(\Omega)}$ and pairwise correlations $\langle \sigma_i \sigma_j \rangle_{P_2(\Omega)}$ with respect to the second-order MEP distribution $P_2(\Omega)$ can be determined by

$$\langle \sigma_i \rangle_{P_2(\Omega)} \equiv \sum_{l=1}^{2^n} \sigma_i(\Omega_l) P_2(\Omega_l),$$

$$\langle \sigma_i \sigma_j \rangle_{P_2(\Omega)} \equiv \sum_{l=1}^{2^n} \sigma_i(\Omega_l) \sigma_j(\Omega_l) P_2(\Omega_l),$$

where $\sigma_i(\Omega_l)$ is the state of the ith node in the network state Ω_l. To improve the agreement between $\langle \sigma_i \rangle_{P_2(\Omega)}$, $\langle \sigma_i \sigma_j \rangle_{P_2(\Omega)}$ and $\langle \sigma_i \rangle_{P(\Omega)}$, $\langle \sigma_i \sigma_j \rangle_{P(\Omega)}$, the values of J_i and J_{ij} are adjusted

by an iterative procedure:

$$J_i^{\text{new}} = J_i^{\text{old}} + \alpha \, \text{sgn}[\langle \sigma_i \rangle_{P(\Omega)}] \log \frac{\langle \sigma_i \rangle_{P(\Omega)}}{\langle \sigma_i \rangle_{P_2(\Omega)}},$$

$$J_{ij}^{\text{new}} = J_{ij}^{\text{old}} + \alpha \, \text{sgn}[\langle \sigma_i \sigma_j \rangle_{P(\Omega)}] \log \frac{\langle \sigma_i \sigma_j \rangle_{P(\Omega)}}{\langle \sigma_i \sigma_j \rangle_{P_2(\Omega)}},$$

where the constant α is used to maintain the stability of the iteration. We use $\alpha = 0.75$ as in Ref. [9].

APPENDIX B: THE HODGKIN-HUXLEY NEURON MODEL

The HH model is described as follows. The dynamics of the membrane potential of the ith neuron, V_i, is governed by [54,55]

$$C \frac{dV_i}{dt} = I_{\text{Na}} + I_K + I_L + I_i^{\text{input}},$$

$$I_{\text{Na}} = -(V_i - V_{\text{Na}})G_{\text{Na}}h_i m_i^3,$$

$$I_K = -(V_i - V_K)G_K n_i^4,$$

$$I_L = -(V_i - V_L)G_L,$$

with

$$\frac{dX_i}{dt} = (1 - X_i)\alpha_X(V_i) - X_i \beta_X(V_i), \tag{B1}$$

where the gating variable $X = m, n, h$ and

$$\alpha_n(V_i) = \frac{0.1 - 0.01V_i}{\exp(1 - 0.1V_i) - 1}, \quad \beta_n(V_i) = \frac{5}{40}\exp(-V_i/80),$$

$$\alpha_m(V_i) = \frac{2.5 - 0.1V_i}{\exp(2.5 - 0.1V_i) - 1}, \quad \beta_m(V_i) = 4\exp(-V_i/18),$$

$$\alpha_h(V_i) = 0.07\exp(-V_i/20), \quad \beta_h(V_i) = \frac{1}{\exp(3 - 0.1V_i) + 1}.$$

The current I_i^{input} describes inputs to the ith neuron coming from the external drive of the network, as well as interactions between neurons in the network, $I_i^{\text{input}} = I_i^E + I_i^I$ with $I_i^E = -(V_i - V_G^E)G_i^E$ and $I_i^I = -(V_i - V_G^I)G_i^I$, where I_i^E and I_i^I are excitatory and inhibitory input currents, respectively, and V_G^E and V_G^I are their corresponding reversal potentials. The dynamics of the conductance, G_i^Q, for $Q = E, I$ are described as follows:

$$\frac{dG_i^Q}{dt} = -\frac{G_i^Q}{\sigma_G^Q} + H_i^Q,$$

$$\frac{dH_i^Q}{dt} = -\frac{H_i^Q}{\sigma_H^Q} + \sum_k F_i^Q \delta(t - T_{i,k}^F) + \sum_{j \neq i} C_{ij} g(V_j^{\text{pre}}),$$

with $g(V_j^{\text{pre}}) = 1/\{1 + \exp[-(V_j^{\text{pre}} - 85)/2]\}$, where F_i^Q is the strength of the external *Poisson input* of rate μ_i to neuron i with $T_{i,k}^F$ being the time of the kth input event. We use $F_i^E = f$, $F_i^I = 0$, $\mu_i = \mu$ for all the neurons in our simulation. The parameter C_{ij} describes the coupling strength from the jth presynaptic neuron to the ith neuron, and V_j^{pre} is the membrane potential of the jth presynaptic neuron. The adjacency matrix, $\mathbf{W} = (w_{ij})$, describes the neuronal network connectivity structure and $C_{ij} = w_{ij}C^{Q_iQ_j}$, where Q_i, Q_j is chosen as E or I, indicating the neuron type of the ith neuron

and the jth neuron ($C^{Q_iQ_j}$ is one of $C^{\text{EE}}, C^{\text{EI}}, C^{\text{IE}}, C^{\text{II}}$). The value $w_{ij} = 1$ if there is a directed coupling from the jth presynaptic neuron to the ith postsynaptic neuron and $w_{ij} = 0$ otherwise.

In this study, the values of parameters in the above conductance equations are chosen as $V_{\text{Na}} = 115\,\text{mV}$, $V_K = -12\,\text{mV}$, $V_L = 10.6\,\text{mV}$ (the resting potential of a neuron is set to 0 mV), $G_{\text{Na}} = 120\,\text{mS cm}^{-2}$, $G_K = 36\,\text{mS cm}^{-2}$, $G_L = 0.3\,\text{mS cm}^{-2}$, the membrane capacity $C = 1\,\mu\text{F cm}^{-2}$, $V_G^E = 65\,\text{mV}$, $V_G^I = -15\,\text{mV}$, $\sigma_G^E = 0.5\,\text{ms}$, $\sigma_H^E = 3.0\,\text{ms}$, $\sigma_G^I = 0.5\,\text{ms}$, and $\sigma_H^I = 7.0\,\text{ms}$. We keep the Poisson input parameters fixed during each single simulation.

In our numerical simulation, an explicit fourth-order Runge-Kutta method is used [54,55] with time step ∼0.03 ms. The spike train data were obtained with a sufficiently high sampling rate, e.g., 2 kHz.

APPENDIX C: PROOF OF ONE-TO-ONE MAPPING BETWEEN THE PROBABILITY DISTRIBUTION AND MOMENTS

We prove that there exists a full-rank matrix $\mathbf{U}_{\text{PM}}^{(n)}$ that transforms from $\mathbf{P}^{(n)}$ to $\mathbf{M}^{(n)}$, i.e.,

$$\mathbf{U}_{\text{PM}}^{(n)} \mathbf{P}^{(n)} = \mathbf{M}^{(n)}, \tag{C1}$$

for a network of any size n. As an illustration with a network of $n = 2$ nodes, the expectation of $\sigma_1, \sigma_2, \sigma_1\sigma_2$ can be obtained by

$$\begin{bmatrix} 1 & 1 & 1 & 1 \\ 0 & 1 & 0 & 1 \\ 0 & 0 & 1 & 1 \\ 0 & 0 & 0 & 1 \end{bmatrix} \begin{bmatrix} P_{00} \\ P_{10} \\ P_{01} \\ P_{11} \end{bmatrix} = \begin{bmatrix} 1 \\ \langle \sigma_1 \rangle \\ \langle \sigma_2 \rangle \\ \langle \sigma_1 \sigma_2 \rangle \end{bmatrix}, \tag{C2}$$

i.e., $\mathbf{U}_{\text{PM}}^{(2)} \mathbf{P}^{(2)} = \mathbf{M}^{(2)}$. Clearly, from Eq. (C2), $\mathbf{U}_{\text{PM}}^{(2)}$ is of full rank. We now prove the above result for any n by mathematical induction. Suppose $\mathbf{U}_{\text{PM}}^{(k)}$ is of full rank. Then $\mathbf{P}^{(k+1)}$ and $\mathbf{M}^{(k+1)}$ can be decomposed into two parts with equal length of 2^k and $\mathbf{U}_{\text{PM}}^{(k+1)}$ can be decomposed into four submatrices with the dimension of each submatrix being $2^k \times 2^k$ as follows:

$$\begin{bmatrix} \mathbf{U}_{11}^{(k+1)} & \mathbf{U}_{12}^{(k+1)} \\ \mathbf{U}_{21}^{(k+1)} & \mathbf{U}_{22}^{(k+1)} \end{bmatrix} \begin{bmatrix} \mathbf{P}_1^{(k+1)} \\ \mathbf{P}_2^{(k+1)} \end{bmatrix} = \begin{bmatrix} \mathbf{M}_1^{(k+1)} \\ \mathbf{M}_2^{(k+1)} \end{bmatrix},$$

where

$$\mathbf{P}_1^{(k+1)} = \begin{bmatrix} P_{000\cdots000} \\ P_{100\cdots000} \\ P_{010\cdots000} \\ P_{110\cdots000} \\ \vdots \\ P_{111\cdots110} \end{bmatrix}, \quad \mathbf{P}_2^{(k+1)} = \begin{bmatrix} P_{000\cdots001} \\ P_{100\cdots001} \\ P_{010\cdots001} \\ P_{110\cdots001} \\ \vdots \\ P_{111\cdots111} \end{bmatrix}.$$

The expression of $\mathbf{M}_1^{(k+1)}$ is the same as the expression of $\mathbf{M}^{(k)}$ in Eq. (6), i.e., $\mathbf{M}_1^{(k+1)} = \mathbf{M}^{(k)}$, and $\mathbf{M}_2^{(k+1)}$ can be expressed

as follows:

$$\mathbf{M}_2^{(k+1)} = \begin{bmatrix} \langle 1 \cdot \sigma_{k+1} \rangle \\ \langle \sigma_1 \sigma_{k+1} \rangle \\ \langle \sigma_2 \sigma_{k+1} \rangle \\ \langle \sigma_1 \sigma_2 \sigma_{k+1} \rangle \\ \vdots \\ \left\langle \sigma_2 \prod_{j=3}^{k} \sigma_j \sigma_{k+1} \right\rangle \\ \left\langle \sigma_1 \sigma_2 \prod_{j=3}^{k} \sigma_j \sigma_{k+1} \right\rangle \end{bmatrix}.$$

In the representation of the base-2 number system of $k + 1$ digits, the first digit of the representation of $i - 1$, indicating the state of node $k + 1$, is 0 for $1 \leqslant i \leqslant 2^k$ and 1 for $2^k + 1 \leqslant i \leqslant 2^{k+1}$. For any i with $1 \leqslant i \leqslant 2^k$, suppose $p_i^{(k)}$ is the probability of state $(\sigma_1, \sigma_2, \ldots, \sigma_k)$, i.e., $P_{\sigma_1 \sigma_2 \cdots, \sigma_k}$, and then the ith entry of $\mathbf{P}_1^{(k+1)}$ and $\mathbf{P}_2^{(k+1)}$ are $P_{\sigma_1 \sigma_2 \cdots, \sigma_k, 0}$ and $P_{\sigma_1 \sigma_2 \cdots, \sigma_k, 1}$, respectively. Thus, the states of nodes from the first to the 2^kth are all the same for $\mathbf{P}^{(k)}$, $\mathbf{P}_1^{(k+1)}$, and $\mathbf{P}_2^{(k+1)}$. Since $\mathbf{M}_1^{(k+1)}$ is the same as $\mathbf{M}^{(k)}$, i.e., their expressions only consider nodes from the first to the 2^kth, the contribution from both $\mathbf{P}_1^{(k+1)}$ and $\mathbf{P}_2^{(k+1)}$ to $\mathbf{M}_1^{(k+1)}$ is the same as the contribution from $\mathbf{P}^{(k)}$ to $\mathbf{M}^{(k)}$, i.e., $\mathbf{U}_{11}^{(k+1)} = \mathbf{U}_{PM}^{(k)}$ and $\mathbf{U}_{12}^{(k+1)} = \mathbf{U}_{PM}^{(k)}$. Since the state of node $k + 1$ is 0 in all entries of $\mathbf{P}_1^{(k+1)}$, there is no contribution of $\mathbf{P}_1^{(k+1)}$ to $\mathbf{M}_2^{(k+1)}$, i.e., $\mathbf{U}_{21}^{(k+1)} = \mathbf{0}$.

Similarly, since the state of node $k + 1$ is 1 in all entries of $\mathbf{P}_2^{(k+1)}$, the contribution from $\mathbf{P}_2^{(k+1)}$ to $\mathbf{M}_2^{(k+1)}$ only depends on the states of nodes from the first to the 2^kth—there is a one-to-one correspondence of each entry between $\mathbf{P}_2^{(k+1)}$ and $\mathbf{P}^{(k)}$ and between $\mathbf{M}_2^{(k+1)}$ and $\mathbf{M}^{(k)}$ as mentioned. Thus, $\mathbf{U}_{22}^{(k+1)} = \mathbf{U}_{PM}^{(k)}$ and we can obtain a *recursive relation*, that is,

$$\mathbf{U}_{PM}^{(k+1)} = \begin{bmatrix} \mathbf{U}_{PM}^{(k)} & \mathbf{U}_{PM}^{(k)} \\ \mathbf{0}^{(k)} & \mathbf{U}_{PM}^{(k)} \end{bmatrix}, \tag{C3}$$

where $\mathbf{0}^{(k)}$ is the zero matrix with dimension $2^k \times 2^k$. Thus, $\mathbf{U}_{PM}^{(k+1)}$ is also a matrix of full rank. By induction, $\mathbf{U}_{PM}^{(n)}$ is of full rank for any n.

APPENDIX D: PROOF OF THE RECURSIVE RELATION AMONG EFFECTIVE INTERACTIONS

For a network of n nodes, we prove the following recursive relation in the full-order MEP analysis using mathematical induction:

$$J_{12\cdots(k+1)} = J_{12\cdots k}^1 - J_{12\cdots k}, \tag{D1}$$

where the term $J_{12\cdots k}^1$ is obtained from the kth-order effective interaction $J_{12\cdots k}$ by changing the state of the $(k + 1)$st node in it.

From the mapping between effective interactions and the probability distribution [Eq. (10)], it can be seen that the effective interactions is simply a linear combination of logarithm of the probability distribution. To express this explicitly, we first introduce the notation H_m^l as

$$H_m^l = \sum_{\Omega \in \Lambda_m^l} \log P(\Omega), \tag{D2}$$

where $\Lambda_m^l = \{(\sigma_1, \sigma_2, \ldots, \sigma_n) | \sum_{i=1}^m \sigma_i = l; \sigma_j = 0, m < j \leqslant n\}$, $0 \leqslant l \leqslant m \leqslant n$.

We *then* show that if the kth-order $(1 \leqslant k \leqslant n)$ effective interaction, $J_{12\cdots k}$, can be expressed as

$$J_{12\cdots k} = \sum_{i=0}^k (-1)^{k-i} H_k^i, \tag{D3}$$

then, Eq. (D1) is also valid as follows. For $1 \leqslant i \leqslant k$, there are i nodes of $k + 1$ nodes active in the states described by H_{k+1}^i of Λ_{k+1}^i. For $0 < i < k + 1$, we can split H_{k+1}^i into two terms; one is H_k^i, where the $(k + 1)$st node is inactive, and the other term is $W_k^{i-1} \equiv H_{k+1}^i - H_k^i$, where the $(k + 1)$st node is active. We also define $W_k^k \equiv H_{k+1}^{k+1}$. If Eq. (D3) can be proved, then we have

$$J_{12\cdots(k+1)} = \sum_{i=0}^{k+1} (-1)^{k+1-i} H_{k+1}^i.$$

By using $H_{k+1}^i = W_k^{i-1} + H_k^i$ and $H_{k+1}^0 = H_k^0$, we finally obtain

$$J_{12\cdots(k+1)} = H_{k+1}^{k+1} + \sum_{i=1}^k (-1)^{k+1-i} \left(W_k^{i-1} + H_k^i \right) - (-1)^k H_{k+1}^0$$

$$= W_k^k + \sum_{i=1}^k (-1)^{k+1-i} W_k^{i-1} - (-1)^k H_{k+1}^0$$

$$- \sum_{i=1}^k (-1)^{k-i} H_k^i$$

$$= \sum_{i=0}^k (-1)^{k-i} W_k^i - \sum_{i=0}^k (-1)^{k-i} H_k^i$$

$$= J_{12\cdots k}^1 - J_{12\cdots k},$$

where $J_{12\cdots k}^1$ is the quantity which switches the state of the $(k + 1)$st node in the kth-order effective interaction $J_{12\cdots k}$ from inactive to active. Therefore, the recursive relation [Eq. (D1)] is proved if Eq. (D3) is valid for $1 \leqslant k \leqslant n$.

We *next* prove the validity of Eq. (D3) by mathematical induction as follows. For $k = 1$, as shown in Eq. (11) in the main text, we have

$$J_1 = \log \frac{P_{10\cdots 0}}{P_{00\cdots 0}}$$

$$= H_1^1 - H_1^0.$$

Therefore, Eq. (D3) is valid when $k = 1$. Now we assume Eq. (D3) is valid for $k \leqslant K$.

We next want to prove that Eq. (D3) holds for $k = K + 1$. We begin by showing that an arbitrary gth-order $(g \leqslant K)$ effective interaction $J_{i_1 \cdots i_g}$ can be expressed as follows:

$$J_{i_1 \cdots i_g} = \sum_{i=0}^g (-1)^{g-i} H_{A_g}^i, \quad g \leqslant K, \tag{D4}$$

where $A_g = \{i_1, \ldots, i_g\}$,

$$H_{A_g}^l = \sum_{\Omega \in \Lambda_{A_g}^l} \log P(\Omega),$$

and $\Lambda_{A_g}^l = \{(\sigma_{i_1}, \sigma_{i_2}, \ldots, \sigma_{i_n}) | \sum_{i_j \in A_g} \sigma_{i_j} = l; \sigma_{i_j} = 0, g < j \leqslant n\}$. To show the validity of Eq. (D4), we can permute the neuronal indexes from $\{1, 2, \ldots, n\}$ to $\{i_1, i_2, \ldots, i_n\}$ by the mapping $j \to i_j$ for $1 \leqslant j \leqslant n$. Since Eq. (D3) is valid for $g \leqslant K$ by assumption, Eq. (D4) is also valid.

Next, we study the relation between $J_{12\cdots(K+1)}$ and the effective interactions whose orders are smaller than $K + 1$. By substituting $\Omega = (1, 1, \ldots, 1, 0, \ldots, 0)$ (nodes from 1 to $K + 1$ are active and nodes from $K + 2$ to n are inactive) into the full-order MEP analysis, we obtain

$$J_{12\cdots(K+1)} + \sum_{g=1}^{K} \sum_{i_1 < \cdots < i_g}^{K+1} J_{i_1 \cdots i_g} = H_{K+1}^{K+1} - H_{K+1}^0. \quad (D5)$$

For $g \leqslant K$, from Eq (D4), by the induction assumption, we have

$$\sum_{i_1 < \cdots < i_g}^{K+1} J_{i_1 \cdots i_g} = \sum_{i=0}^{g} (-1)^{g-i} C_{K+1-i}^{g-i} H_{K+1}^i, \quad (D6)$$

where C_{K+1-i}^{g-i} is the number of the selection of $g - i$ terms from all the possible $K + 1 - i$ choices. Since $J_{i_1 \cdots i_g}$ is the gth-order effective interaction, as in Eq. (D4), the sign of the logarithm probability of a state in which there are i nodes active is $(-1)^{g-i}$. To consider the coefficient of H_{K+1}^i in the right-hand side of Eq. (D6), we can consider that for each group of i nodes, how many groups of g nodes in the left-hand side of Eq. (D6) containing these considered i nodes, where $g \geqslant i$. If there are g nodes containing the considered i nodes, then there are only $g - i$ nodes unknown. These $g - i$ nodes can be chosen from the group of nodes which belongs to the total $K + 1$ nodes but not the considered i nodes. Therefore, the choice number of these $g - i$ nodes is C_{K+1-i}^{g-i}. Then we have

$$J_{12\cdots(K+1)} = H_{K+1}^{K+1} - H_{K+1}^0 - \sum_{g=1}^{K} \sum_{i=0}^{g} (-1)^{g-i} C_{K+1-i}^{g-i} H_{K+1}^i. \quad (D7)$$

For $K + 1 > l > 0$, the coefficient of H_{K+1}^l is

$$-\sum_{g=l}^{K} (-1)^{g-l} C_{K+1-l}^{g-l} = (-1)^{K+1-l}. \quad (D8)$$

The coefficient of H_{K+1}^0 is

$$-1 - \sum_{g=1}^{K} (-1)^g C_{K+1}^g = (-1)^{K+1}. \quad (D9)$$

Through Eqs. (D7), (D9), and (D8), we obtain

$$J_{12\cdots(K+1)} = \sum_{i=0}^{K+1} (-1)^{K+1-i} H_{K+1}^i. \quad (D10)$$

That is, Eq. (D3) is valid for $k = K + 1$. By induction, we obtain that Eq. (D3) holds for any integer k with $1 \leqslant k \leqslant n$. Therefore, we prove the validity of Eq. (D1).

APPENDIX E: THE RECURSIVE RELATION OBTAINED DIRECTLY FROM THE ONE-TO-ONE MAPPING

With the one-to-one mapping, the recursive relation can also be obtained. Similarly as the proof of the one-to-one mapping between the probability distribution and the moments, we have

$$\mathbf{L}_{JP}^{(k+1)} \mathbf{J}^{(k+1)} = \log \mathbf{P}^{(k+1)},$$

with

$$\mathbf{L}_{JP}^{(k+1)} = \begin{bmatrix} \mathbf{L}_{JP}^{(\mathbf{k})} & \mathbf{0}^{(k)} \\ \mathbf{L}_{JP}^{(k)} & \mathbf{L}_{JP}^{(k)} \end{bmatrix},$$

$$\mathbf{J}^{(k+1)} = \begin{bmatrix} \mathbf{J}^{(k)} \\ \mathbf{J}^{(k)'} \end{bmatrix},$$

$$\mathbf{P}^{(k+1)} = \begin{bmatrix} \mathbf{P}^{(k)} \\ \mathbf{P}^{(k)'} \end{bmatrix},$$

where the ith element in $\mathbf{J}^{(k)'}$ includes the $(k + 1)$st neuron compared with the ith element in $\mathbf{J}^{(k)}$, similarly to the situation discussed in Appendix C, e.g., the second element in $\mathbf{J}^{(k)}$ is J_1 and in $\mathbf{J}^{(k)'}$ is $J_{1,k+1}$; the ith element in $\mathbf{P}^{(k)'}$ includes the $(k + 1)$st neuron's firing compared with the ith element in $\mathbf{P}^{(k)}$, e.g., the second element in $\mathbf{P}^{(k)}$ is $P_{010\cdots00}$ while that in $\mathbf{P}^{(k)'}$ is $P_{010\cdots01}$. Then

$$\mathbf{J}^{(k+1)} = \begin{bmatrix} \mathbf{J}^{(k)} \\ \mathbf{J}^{(k)'} \end{bmatrix} = \begin{bmatrix} \left(\mathbf{L}_{JP}^{(k)}\right)^{-1} & \mathbf{0}^{(k)} \\ -\left(\mathbf{L}_{JP}^{(k)}\right)^{-1} & \left(\mathbf{L}_{JP}^{(k)}\right)^{-1} \end{bmatrix} \begin{bmatrix} \log \mathbf{P}^{(k)} \\ \log \mathbf{P}^{(k)'} \end{bmatrix}.$$

Denote

$$\mathbf{J}_1^{(k)} \triangleq \left(\mathbf{L}_{JP}^{(k)}\right)^{-1} \log \mathbf{P}^{(k)'},$$

and we have

$$\mathbf{J}^{(k)'} = \mathbf{J}_1^{(k)} - \mathbf{J}^{(k)}, \quad (E1)$$

which corresponds to the relation in Eq. (13). Therefore, we have proved the recursive relation of Eq. (13).

APPENDIX F: ELECTROPHYSIOLOGICAL EXPERIMENTS

The data were collected in the Laboratory of Adam Kohn at the Albert Einstein College of Medicine and downloaded [38]. These data consist of multielectrode recordings from V1 in anesthetized macaque monkeys, while natural images and gratings were flashed on the screen as visual stimuli. Recordings were performed using the "Utah" electrode array and spike-sorting algorithm was used to determine spike trains corresponding to each single neuron. Natural images were presented at two sizes, $3°$–$6.7°$ and windowed to $1°$, to quantify surround modulation. All stimuli (956 in total) were displayed in pseudorandom order for 100 ms each, followed by a 200-ms uniform gray screen. Each stimulus was presented 20 times. Experimental procedures and stimuli are fully described in Ref. [37].

[1] E. Schneidman, M. J. Berry, R. Segev, and W. Bialek, Nature **440**, 1007 (2006).

[2] J. Shlens, G. D. Field, J. L. Gauthier, M. I. Grivich, D. Petrusca, A. Sher, A. M. Litke, and E. Chichilnisky, J. Neurosci. **26**, 8254 (2006).

[3] Z.-Q. J. Xu, G. Bi, D. Zhou, and D. Cai, Commun. Math. Sci. **15**, 665 (2017).

[4] D. C. Knill and A. Pouget, Trends Neurosci. **27**, 712 (2004).

[5] M. P. Karlsson and L. M. Frank, Nat. Neurosci. **12**, 913 (2009).

[6] A. S. Morcos and C. D. Harvey, Nat. Neurosci. **19**, 1672 (2016).

[7] E. T. Jaynes, Phys. Rev. **106**, 620 (1957).

[8] G. Tkacik, E. Schneidman, I. Berry, J. Michael, and W. Bialek, arXiv:q-bio/0611072.

[9] A. Tang, D. Jackson, J. Hobbs, W. Chen, J. L. Smith, H. Patel, A. Prieto, D. Petrusca, M. I. Grivich, A. Sher *et al.*, J. Neurosci. **28**, 505 (2008).

[10] D. Sakakibara, A. Sasaki, T. Ikeya, J. Hamatsu, T. Hanashima, M. Mishima, M. Yoshimasu, N. Hayashi, T. Mikawa, M. Wälchli *et al.*, Nature **458**, 102 (2009).

[11] J. I. Sułkowska, F. Morcos, M. Weigt, T. Hwa, and J. N. Onuchic, Proc. Natl. Acad. Sci. USA **109**, 10340 (2012).

[12] A. B. Mantsyzov, A. S. Maltsev, J. Ying, Y. Shen, G. Hummer, and A. Bax, Prot. Sci. **23**, 1275 (2014).

[13] S. Saremi and T. J. Sejnowski, Proc. Natl. Acad. Sci. USA **110**, 3071 (2013).

[14] A. Golan, G. G. Judge, and D. Miller, *Maximum Entropy Econometrics: Robust Estimation with Limited Data* (Wiley, New York, 1996).

[15] T. Squartini, I. van Lelyveld, and D. Garlaschelli, Sci. Rep. **3**, 3357 (2013).

[16] G. J. Stephens and W. Bialek, Phys. Rev. E **81**, 066119 (2010).

[17] A. Hernando, R. Hernando, A. Plastino, and A. Plastino, J. R. Soc. Interface **10**, 20120758 (2013).

[18] S. Khatiwala, F. Primeau, and T. Hall, Nature **462**, 346 (2009).

[19] E. Ganmor, R. Segev, and E. Schneidman, Proc. Natl. Acad. Sci. USA **108**, 9679 (2011).

[20] I. E. Ohiorhenuan, F. Mechler, K. P. Purpura, A. M. Schmid, Q. Hu, and J. D. Victor, Nature **466**, 617 (2010).

[21] S. Yu, H. Yang, H. Nakahara, G. S. Santos, D. Nikolić, and D. Plenz, J. Neurosci. **31**, 17514 (2011).

[22] Y. Roudi, S. Nirenberg, and P. E. Latham, PLoS Comput. Biol. **5**, e1000380 (2009).

[23] J. H. Macke, M. Opper, and M. Bethge, Phys. Rev. Lett. **106**, 208102 (2011).

[24] A. K. Barreiro, J. Gjorgjieva, F. Rieke, and E. Shea-Brown, Front. Comput. Neurosci. **8**, 10 (2014).

[25] H. Shimazaki, K. Sadeghi, T. Ishikawa, Y. Ikegaya, and T. Toyoizumi, Sci. Rep. **5**, 9821 (2015).

[26] L. Merchan and I. Nemenman, J. Stat. Phys. **162**, 1294 (2016).

[27] G. Tkačik, O. Marre, D. Amodei, E. Schneidman, W. Bialek, and M. J. Berry II, PLoS Comput. Biol. **10**, e1003408 (2014).

[28] J. Humplik and G. Tkačik, PLoS Comput. Biol. **13**, e1005763 (2017).

[29] N. Cayco-Gajic, J. Zylberberg, and E. Shea-Brown, Entropy **20**, 489 (2018).

[30] T. Bury, Eur. Phys. J. B **86**, 89 (2013).

[31] A. Cavagna, I. Giardina, F. Ginelli, T. Mora, D. Piovani, R. Tavarone, and A. M. Walczak, Phys. Rev. E **89**, 042707 (2014).

[32] D. Zhou, Y. Xiao, Y. Zhang, Z. Xu, and D. Cai, PLoS ONE **9**, e87636 (2014).

[33] S.-i. Amari, IEEE Trans. Inf. Theory **47**, 1701 (2001).

[34] T. Obuchi and R. Monasson, J. Phys.: Conf. Ser. **638**, 012018 (2015).

[35] R. De Wolf, Theory Comput. Grad. Surv. **1**, 15 (2008).

[36] E. Ganmor, R. Segev, and E. Schneidman, J. Neurosci. **31**, 3044 (2011).

[37] R. Coen-Cagli, A. Kohn, and O. Schwartz, Nat. Neurosci. **18**, 1648 (2015).

[38] A. Kohn and R. Coen-Cagli (2015), Multi-electrode recordings of anesthetized macaque V1 responses to static natural images and gratings, http://dx.doi.org/10.6080/K0SB43P8.

[39] H. Nasser, O. Marre, and B. Cessac, J. Stat. Mech.: Theory Exp. (2013) P03006.

[40] T. Broderick, M. Dudik, G. Tkacik, R. E. Schapire, and W. Bialek, arXiv:0712.2437.

[41] J. Shlens, F. Rieke, and E. Chichilnisky, Curr. Opin. Neurobiol. **18**, 396 (2008).

[42] O. Marre, S. El Boustani, Y. Frégnac, and A. Destexhe, Phys. Rev. Lett. **102**, 138101 (2009).

[43] F.-C. Yeh, A. Tang, J. P. Hobbs, P. Hottowy, W. Dabrowski, A. Sher, A. Litke, and J. M. Beggs, Entropy **12**, 89 (2010).

[44] H. Nasser and B. Cessac, Entropy **16**, 2244 (2014).

[45] S. Yu, D. Huang, W. Singer, and D. Nikolić, Cerebr. Cortex **18**, 2891 (2008).

[46] Y. Roudi, J. Tyrcha, and J. Hertz, Phys. Rev. E **79**, 051915 (2009).

[47] J. Hertz, Y. Roudi, and J. Tyrcha, arXiv:1106.1752.

[48] T. Watanabe, S. Hirose, H. Wada, Y. Imai, T. Machida, I. Shirouzu, S. Konishi, Y. Miyashita, and N. Masuda, Nat. Commun. **4**, 1370 (2013).

[49] J. Barton and S. Cocco, J. Stat. Mech.: Theory Exp. (2013) P03002.

[50] B. Dunn, M. Mørreaunet, and Y. Roudi, PLoS Comput Biol. **11**, e1004052 (2015).

[51] J. Zhang, K. Newhall, D. Zhou, and A. Rangan, J. Comput. Neurosci. **36**, 279 (2014).

[52] J. Zhang, D. Zhou, D. Cai, and A. V. Rangan, J. Comput. Neurosci. **37**, 81 (2014).

[53] J. Shlens, G. D. Field, J. L. Gauthier, M. Greschner, A. Sher, A. M. Litke, and E. Chichilnisky, J. Neurosci. **29**, 5022 (2009).

[54] Y. Sun, D. Zhou, A. V. Rangan, and D. Cai, J. Comput. Neurosci. **27**, 369 (2009).

[55] Y. Sun, D. Zhou, A. Rangan, and D. Cai, J. Comput. Neurosci. **28**, 247 (2010).